Thermodynamic stability and electronic structure of pristine wurtzite ZnO{0001} inversion domain boundaries

Jochen Rohrer◉ and Karsten Albe◉

Institut für Materialwissenschaft, Technische Universität Darmstadt, Otto-Berndt-Strasse 3, 64287 Darmstadt, Germany

Recently, it was demonstrated that the conductivity of wurtzite (wz) ZnO bicrystal samples containing {0001} inversion domain boundaries (IDB) can be massively and reversibly tuned by mechanical loading. As a step towards a detailed microscopic understanding of this effect, we systematically investigate the atomic structure and chemical composition of such IDBs using density functional theory calculations. In total, 92 model geometries that differ in structure and/or chemical composition are constructed, optimized, and compared thermodynamically. The lack of higher symmetries in wz ZnO prohibits a straightforward calculation of individual grain boundary (GB) excess energies. However, we show that, in nonperiodic slab models of wz {0001} IDBs, the additional surface contribution to the total energy may be approximated by that of corresponding zincblende (zb) surfaces; the latter can be obtained by a series of prism calculations. Subtracting these surface energies allows us to construct absolute GB energy diagrams for wz IDBs and compare their thermodynamic stability with other GBs known from the literature. We find that thermodynamically favored IDBs are characterized by fully (4-fold) coordinated atoms and possess relatively low excess energies that range from 45 to 95 meV/Å^2, depending on the termination (Zn/Zn or O/O) of the IDB and the exchange-correlation functional used in the calculation (LDA, GGA, or GGA+U). The electronic properties of the GB deviate only weakly from those of the bulk and are rather insensitive towards compressive and tensile strains. Our results thus indicate that experimentally observed piezotronic properties of wz bicrystals are not an intrinsic property of the pristine GB itself, but originate, for example, from externally supplied trapped charges, defects, impurities, or dopants. Low-energy structure models identified here may also be transferable to other wz- or zb-type IDBs (e.g., GaN, AlN, SiC, etc.).

I. INTRODUCTION

Zinc oxide [1] is widely used in light-emitting devices [2], photodiodes [3], thin-film transistors [4], and varistor devices [5]. More recently, ZnO has also attracted interest due to the piezotronic effect where stress-induced piezoelectric charge modulates the electrostatic barrier height at grain boundaries (GB) and thus their resistivity [6]. This work triggered a series of studies investigating the mechanical tunability of the resistivity for strain-sensing applications using metal/ZnO nanowire systems [7–13] and ZnO polycrystals [14–17]. However, while for metal/ZnO nanowire systems only moderate changes in the potential barrier were achieved, polycrystals pose the difficulty of precisely controling electrical and structural parameters.

A particular promising piezotronic system was recently proposed by Keil *et al.* [18]. They used an epitaxial solid-state transformation to synthesize ZnO bicrystals. These bicrystals consist of two domains that are aligned along the *c* axis, separated by {0001} inversion domain boundaries (IBDs) with head-to-head (O/O) or tail-to-tail (Zn/Zn) polarizations. By applying a mechanical load of up to 250 MPa, a variation of the current over two orders of magnitude was demonstrated and rationalized by variations of the electrostatic potential barriers [19] at the inversion domain boundaries.

In this work we address structure, thermodynamics, and electronic properties of ZnO IDBs relevant for piezotronic

ZnO bicrystals using density functional theory (DFT) calculations. Despite the sizable amount of theoretical studies focusing on pristine, defective or doped tilt GBs in ZnO [20–24], studies concerning {0001} IDBs are rare and narrow concerning variations of the chemical composition and associated atomic structure [25] or focus on specific dopants that facilitate growth of such IDBs [26,27]. Here we construct a variety of pristine IDB models by contacting two Zn (O) terminated {0001} surfaces via an O (Zn) interlayer. By varying the coverage of the interlayer and the detailed stacking along the *c* axis, we construct a GB phase diagram and subsequently investigate electronic properties of favorable models, in particular with respect to strain.

We find that thermodynamically favorable IDB models are characterized by the exclusive presence of 4-fold coordinated atoms, that is, no over or undercoordinated atoms are present atoms at the GB. At the Zn/Zn boundary at high O chemical potential, two more chemically and structurally different GB modifications may be stabilized. The calculated excess energies of all favored models are comparable or even below those of many special GBs. The electronic structure variations with respect to strain are marginal, suggesting that the mechanically tunable resistivty of bicrystals is governed by trapped additional charges (supplied by applying a potential difference), defects, impurities, or dopants.

This paper is organized as follows. In Sec. II we summarize the computational method and our modeling approach. In

TABLE I. Comparison of experimental and calculated lattice parameters and band gaps for wurtzite and zincblende ZnO. The Hubbard U values are chosen such that, for wurtzite, a minmum (relative) mean-square deviation between experimental and calculated lattice parameters is obtained ($U_{PBE} = 4$, $U_{revPBE} = 5.95$, $U_{RPBE} = 6.67$), see also Fig. S2.

| | | LDA | GGA | | | GGA+U | | | Hybrid | |
	Expt.	VWN	PBE	revPBE	RPBE	PBE+U	revPBE+U	RPBE+U	B3LYP	PBE0
					wurtzite					
a (Å)	3.25	3.195	3.286	3.314	3.325	3.242	3.242	3.241	3.283	3.256
c (Å)	5.20	5.160	5.301	5.344	5.361	5.223	5.219	5.217	5.288	5.231
E_{gap} (eV)	3.22	0.80	0.72	0.75	0.77	1.30	1.60	1.72	2.75	3.13
					zincblende					
a (Å)	4.580	4.500	4.627	–	–	–	–	4.560	–	4.578
E_{gap} (eV)	3.12	0.70	0.62	–	–	–	–	1.60	–	2.97

Sec. III we present and discuss our results on surface and grain boundary stability and analyze electronic properties (effective potential, Bader charges, and atom-projected density of states) with particular focus on variations upon mechanical loading. Our conclusions are given in Sec. IV. In addition, Supplemental Material [28] with further detailed presentations of various aspects of this work exists.

II. METHOD

A. Computational details

All calculations are performed on the basis of density functional theory (DFT) using the plane-wave projector augmented-wave code vasp [29,30]. As detailed in Fig. S1 in the Supplemental Material [28], we performed a careful convergence study for bulk ZnO. We find that energy differences are converged to 0.1 meV/atom or better for a plane-wave cutoff of 700 eV and a Γ-centered $N_1 \times N_2 \times N_3$ Monkhorst-Pack k-mesh [31] with $N_i \cdot a_i \approx 32$ Å, where N_i is an integer and a_i is the length of the ith lattice vector. We generally use a Fermi smearing with standard smearing width. For supercells that include vacuum along the c axis, a $N_1 \times N_2 \times 1$ sampling is used. In all calculations electronic self-consistency is considered to be reached as the change in total energy between iterations is lower than 10^{-7} eV; structure optimizations are stopped once the maximum force on individual atoms is below 0.01 eV/Å.

Using these parameters, we subsequently screen various XC functionals (LDA [32], GGA (PBE [33], revPBE [34], RPBE [35]), PBE0 [36], B3LYP [37], and GGA+U [38] [PBE+U, revPBE+U, and RPBE+U]) regarding their performance in reproducing the experimental lattice parameters and band gap, see Table I. For the GGA+U functionals, the Hubbard U parameters are determined by minimizing the deviations of calculated from experimental lattice parameters. For details, see Fig. S2 in the Supplemental Material [28]. The optimal agreement with respect to experiment is obtained for the PBE0 functional. However, for larger IDB systems, using hybrid functionals such as PBE0 is challenging and requires a vast amount of computational resources. In this work, we therefore restrict ourselves to computationally more efficient functionals. Among these, the RPBE+U functional (with $U = 6.67$) is chosen as it yields the best agreement with experiment. For comparison, we also use parameter-free LDA and GGA (in the version of PBE).

B. Atomic structure of inversion domain boundaries

To model IDBs, we use nonperiodic bicrystals with two additional surfaces and a vacuum layer of 12 Å thickness. The bicrystals consist of two {0001} grains, each of which contains 12 atomic layers, and are contacted via an interlayer. We emphasize that, despite the seeming simplicity of such IDBs, there is a significant amount of complexity in the structural and compositional degrees of freedom.

The left panel of Fig. 1 shows the various high-symmetry configurations in which two {0001} oriented grains may be stacked on top of each other. The first grain is always fixed in a ...*BABA* stacking. The second grain is obtained by mirroring the first at the {0001} plane, an additional rotation $\hat{R}$ by $0°$ or $180°$ around the **c** axis through an A site and a final translation $\hat{T}$ of $0 \cdot \mathbf{d}$, $1/3 \cdot \mathbf{d}$ or $-1/3 \cdot \mathbf{d}$, where $\mathbf{d} = \mathbf{a} + \mathbf{b}$ and $\mathbf{a}$, $\mathbf{b}$ are the in-plane lattice vectors. The effects of these operations are $\hat{T} : A \to B, B \to C, C \to A, \quad -\hat{T} : A \to C, B \to A, C \to B, \quad \text{and} \quad \hat{R} : A \to A, B \to C, C \to B$, respectively. We note that, by applying these operations to the combined bicrystal, it is straightforward to show that only five out of the six models shown in the left panel of Fig. 1 are symmetrically distinct, see Table S1 in the Supplemental Material [28].

Further structural complexity arises, when considering the possibility of an interlayer at the GB, see right panel of Fig. 1. Available sites for the interlayer considered in this work are the top, hcp, and fcc (or hollow) sites relative to the lower grain.

Finally, the coverage θ of the interlayer may be varied, adding a compositional complexity to our GB models. Variation of the interlayer coverage is achieved using different in-plane repetition units. Here we consider 1×1, $\sqrt{3} \times \sqrt{3}$, 2×2, and $\Sigma 7$ twist models with fractional occupation θ of the interlayer sites. This allows us to construct IDB models with $\theta = 0$ (1×1 cell with no interlayer), $\theta = 1/3$ ($\sqrt{3} \times \sqrt{3}$ cell with interlayer atoms occupying one out of the three available sites), $\theta = 1/2$ (2×2 cell with interlayer atoms occupying two out of the four available sites), and $\theta = 1$ (1×1 cell with interlayer); $\Sigma 7$ models (not shown in Fig. 1) allow further for $\theta = 3/7$ and $\theta = 4/7$ and are considered here since experimental bicrystal samples show the presence of a small twist [18]. For 1×1 models all possible (symmetrically distinct) structure models are considered; for larger in-plane repeat units, only selected structural models are considered.
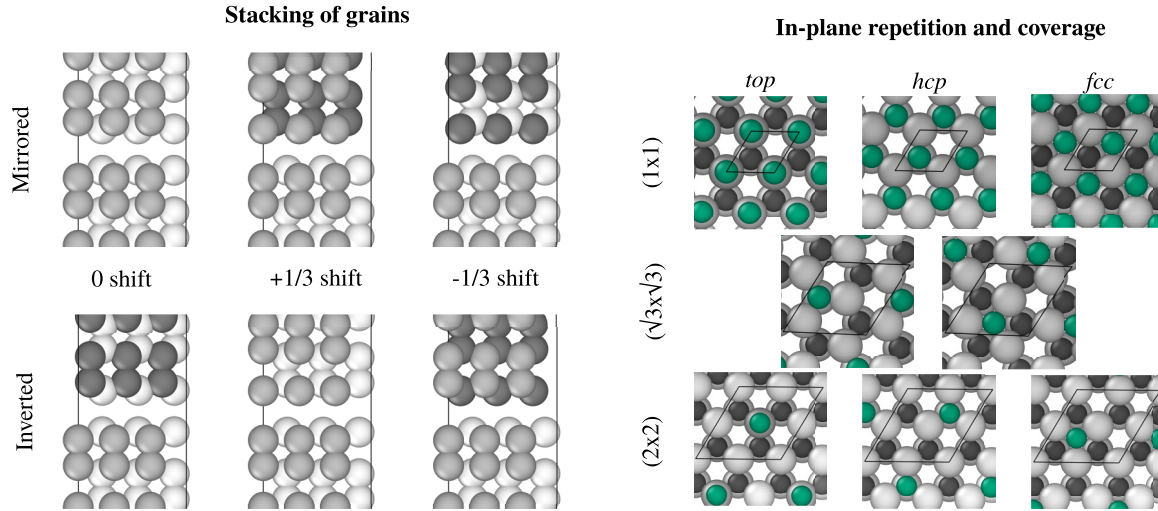
Stacking of grains   **In-plane repetition and coverage**

FIG. 1. Structure and composition of inversion domain boundaries (IDB). (Left) All grain-boundary models are constructed by contacting two wz{0001} grains. The first grain is aligned along the (0001) or along the (000$\bar{1}$) direction and terminated by a three-fold coordinated layer. By definition the stacking is . . . *BABA*. Different sites are distinguished by different colors; we do not distinguish between Zn/O. The second grain is obtained by mirroring grain 1 at the {0001} plane; in addition the second grain may be rotated by 180° around the *c* axis through an *A* site and translated by 1/3 or 2/3 along the diagonal of the 1×1 cell. (Right) An interlayer (indicated by dark green spheres) is added between the two grains in various sites. This interlayer may be fully or partially occupied, leading to chemically different GBs. Partial occupancy is achieved using different in-plane repeat units.

In these models, we aim at minimizing the number of falsely coordinated atoms.

C. Surface termination and electronic structure

Truncating the wurtzite structure at a {0001} plane leaves one undercoordinated Zn/O atom at the surface. This leads to additional surface states that shift the valence-band maximum and thus the Fermi level in the DFT calculations to higher energies. Moreover, the surface states may interact with states localized at the IDB which can influence the energetics. Such effects can be minimized by proper surface saturation. In Sec. III of the Supplemental Material [28] we present a careful analysis of the effect of saturating ZnO{0001} surfaces in various ways, see specifically, Figs. S3 and S4. We find that surface saturation using pseudo-H with 1/2 (at the O-terminated surface) and 3/2 valence electrons (at the Zn-terminated surface) yields electronic properties that agree well with those of a periodic model (containing two nonequivalent IDBs). This surface saturation was thus chosen for all IDB calculations presented in this work.

III. RESULTS AND DISCUSSION

In total, 92 IDB models were constructed and optimized (half of which are Zn/Zn and half of which are O/O boundaries). In Fig. S5 we show that, for fixed composition/coverage, the energy variation and, in particular, the lowest-energy structures are independent of the choice of the XC functional. The lowest-energy configurations for each coverage and orientation are shown in Fig. S6. In the following we will address the thermodynamic stability of the various models and analyze the atomic and electronic structure of favorable ones.

A. Thermodynamics of IDB

Based on the total energies $E_{\theta,0}$ of the most favorable configurations for each orientation and coverage, the absolute GB energy is

$$\gamma_\theta^{\text{X/X}}(\mu_O) = [E_{\theta,0} - n_{\text{Zn}}\epsilon_{\text{ZnO}} - (n_O - n_{\text{Zn}})\mu_O]/A$$
$$- 2A\sigma_{(0001)}^{\text{Y}}(\mu_O). \quad (1)$$

Here the superscript label X/X indicates a Zn/Zn or O/O IDB (X = Zn or O), n_{Zn} and n_O is the number of Zn and O atoms in the bicrystal, ϵ_{ZnO} is the total energy per formula unit (f.u.) of the bulk, μ_O is the chemical potential of O, *A* is the GB contact area (per cell) and $\sigma_{(0001)}^{\text{Y}}$ is the excess energy of a Y terminated wz(0001) surface (Y is complementary to X).

The main issue in evaluating Eq. (1) for wz IDBs is the fact that $\sigma_{(0001)}^{\text{Y}}$ cannot be easily computed for individual terminations. In the following subsection, we will first show that $\sigma_{(0001)}^{\text{Y}}$ may be repalced by $\sigma_{(111)}^{\text{Y}}$ of the zincblende (zb) phase, without introducing significant errors. For zb, $\sigma_{(111)}^{\text{Y}}$ is then obtained individually from a set of prism calculations. After this excursion to surface energies, we eventually return to the stability of GBs in Sec. III A 2.

1. Excursion-Surface excess energies

Figure 2 compares the average excess energy of wz{0001} and zb{111} surfaces (averaged over both terminations) as obtained from a series of slab calculations, using stoichiometric slabs (having both a Zn and an O terminated surface) and various XC functionals. The average excess energy is defined as

$$\bar{\sigma}_n = (E_n - n\epsilon_{\text{f.u.}})/2A, \quad (2)$$

where E is the total energy of the slab containing n f.u., $\epsilon_{\text{f.u.}}$ is the total energy per formula unit of wz or zb bulk, and
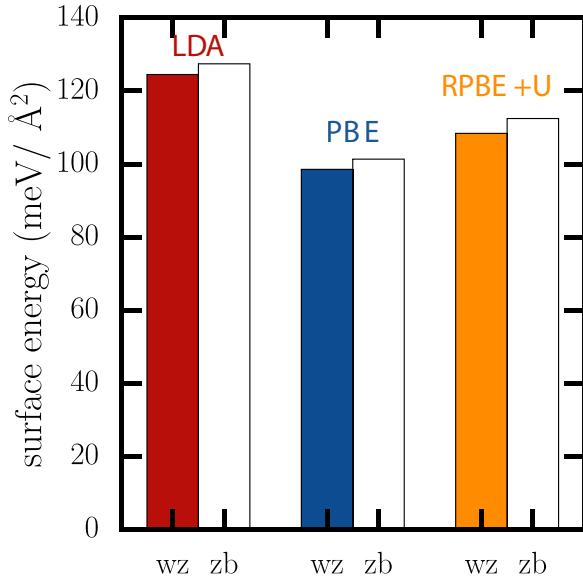
FIG. 2. Surface energies (average over both terminations/sides) of wz(0001) and zb(111) calculated using LDA (left), PBE (middle), and RPBE+U (right). Independent of the XC functional, both surfaces show almost identical excess energies.

A is the surface area of the supercell. We find that, independent of the XC functional, the two ZnO phases exhibit almost identical surface energies—with roughly $\bar{\sigma}_{\text{wz}(0001)} = \bar{\sigma}_{\text{zb}(111)} - 5$ meV/Å^2. This, together with the fact that wz and zb are structurally very similar, suggests that replacing

$$\sigma_{\text{wz}(0001)}^{\text{Zn}} \approx \sigma_{\text{zb}(111)}^{\text{Zn}} - 2.5 \text{ meV/Å}^2, \quad (3)$$

$$\sigma_{\text{wz}(0001)}^{\text{O}} \approx \sigma_{\text{zb}(111)}^{\text{O}} - 2.5 \text{ meV/Å}^2, \quad (4)$$

will only introduce minor errors in the calculation of grain boundary energies from nonperiodic bicrystals.

The surface energies of Zn and O terminated zb(111) can be obtained from a series of prism calculations [39–41]. Figure 3 shows various stoichiometric prisms (no Zn excess or deficiency) that contain two Zn terminated (111) and one O terminated (001) surface (Zn-O-Zn prisms). The total energy of such a Zn-O-Zn prism is given by

$$E_{\text{Zn-O-Zn}}(n) = n\epsilon_{\text{zb}} + 2A_{(111)}\sigma_{(111)}^{\text{Zn}} + A_{(001)}\sigma_{(001)}^{\text{O}}$$
$$+ l_{\text{rep}}\eta_{(111)/(111)} + 2l_{\text{rep}}\eta_{(111)/(001)}. \quad (5)$$

Here, n is the number of formula units of ZnO, ϵ_{zb} is the total energy per formula unit of bulk zb-ZnO, $2A_{(111)}$ is the total area of the two factes with (111) orientation, $A_{(001)}$ is the area of the (001) facet, $\sigma_{(111)}^{\text{Zn}}$ and $\sigma_{(001)}^{\text{O}}$ are the corresponding surface excess energies, l_{rep} is the repeat length of the prism, and $\eta_{(111)/(111)}$ and $\eta_{(111)/(001)}$ are edge excess energies at (111)/(111) and (111)/(001) edges, respectively. Obviously, we can also construct O-Zn-O prisms that contain two O terminated (111) and one Zn terminated (001) surface; the above and following equations can then to be adapted by exchanging $\sigma_{(111)}^{\text{Zn}}$ by $\sigma_{(111)}^{\text{O}}$ and $\sigma_{(001)}^{\text{O}}$ by $\sigma_{(001)}^{\text{Zn}}$.
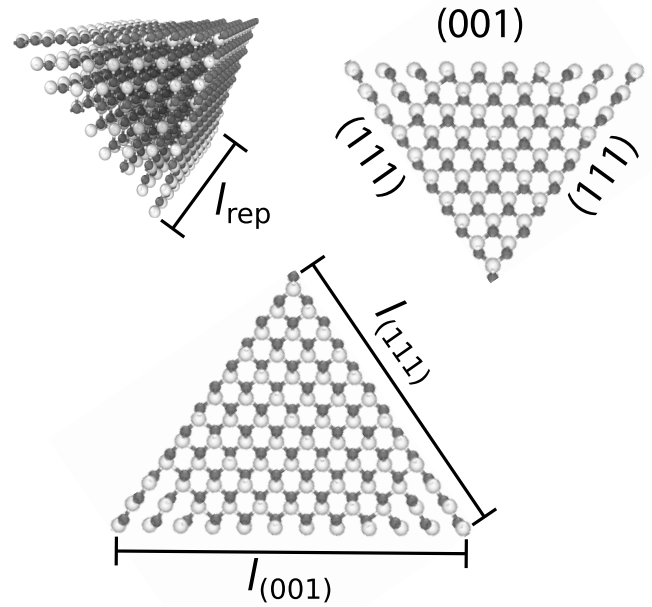

FIG. 3. Zincblende prisms containing two Zn terminated (111) and one O terminated (001) surface. Overall the prisms contain no Zn excess or deficiency. The total excess energy of such a prism consists of the excess of the surfaces and of the three edges. As the size of the prism increases, the surface excess becomes more and more dominant and can be extracted for the limit of an infinitely large prism.

We next define the size-dependent excess energy of a prism as

$$\Delta E_{\text{Zn-O-Zn}}^{\text{exc}}(n) = E_{\text{total}} - n\epsilon_{\text{zb}}$$
$$= 2A_{(111)}\sigma_{(111)}^{\text{Zn}} + A_{(001)}\sigma_{(001)}^{\text{O}}$$
$$+ l_{\text{rep}}(\eta_{(111)/(111)} + 2\eta_{(111)/(001)}). \quad (6)$$

By normalizing $\Delta E_{\text{Zn-O-Zn}}^{\text{exc}}(n)$ with the total area of (111) facets, and realizing that $A_{(111)} \propto l_{\text{rep}}l_{(111)}$ with $l_{(111)}$ being the side length of a (111) facet, we see that the resulting quantity $\Delta\epsilon_{\text{Zn-O-Zn}}^{\text{exc}}(n) = \Delta E_{\text{prism}}^{\text{exc}}(n)/2A_{(111)}$ behaves as

$$\Delta\epsilon_{\text{Zn-O-Zn}}^{\text{exc}}(n) = \Delta\epsilon_{\text{Zn-O-Zn}}^{\text{exc},\infty} + C/l_{(111)}, \quad (7)$$

where $\Delta\epsilon_{\text{prism}}^{\text{exc},\infty}$ and C are constants. In particular, the numerical values of the edge excess energies are projected out and we can directly construct the μ-dependent surface-energy diagram of zb(111) using

$$\sigma_{(111)}^{\text{Zn}}(\mu_{\text{O}}) = \Delta\epsilon_{\text{Zn-O-Zn}}^{\text{exc},\infty} - \frac{A_{(001)}}{2A_{(111)}}\sigma_{(001)}^{\text{O}}(\mu_{\text{O}}), \quad (8)$$

and similarly for $\sigma_{(111)}^{\text{O}}$ using O-Zn-O prisms. Note that, for geometric reasons, $A_{(001)}/2A_{(111)} = 1/\sqrt{3}$. We further emphasize that, for surfaces with inversion symmetry, the slope of the surface energy is always $S = \Delta n_X/2A$. Here, the slope is $(\Delta n_X/2A_{(001)})(A_{(001)}/2A_{(111)}) = \Delta n_X/4A_{(111)}$ and thus only half as large.

Figure 4 shows the variation of $\Delta\epsilon_{\text{prism}}^{\text{exc}}(n)$ for both Zn-O-Zn and O-Zn-O prisms. For LDA and PBE corresponding
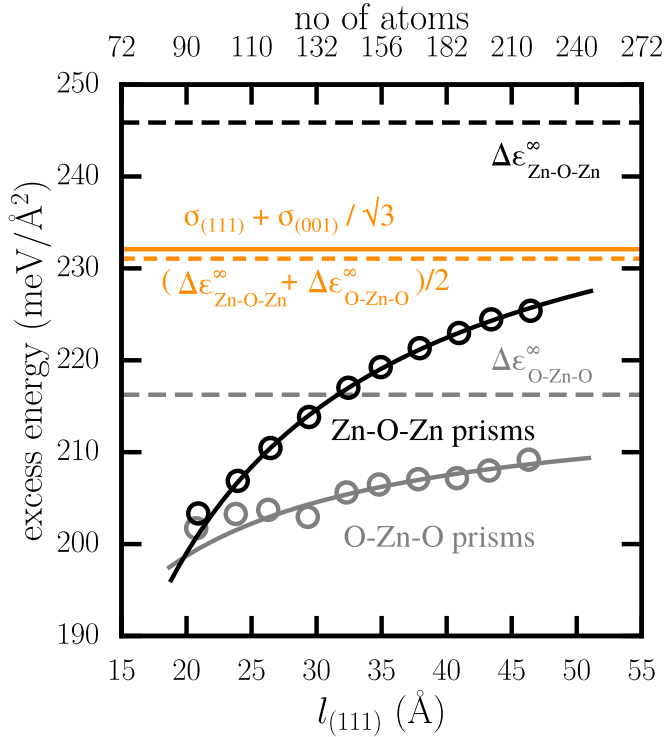
FIG. 4. Excess energies of zb prisms as obtained from a series of calculations using the RPBE+U XC functional. Prisms containing Zn terminated (111) facets (Zn-O-Zn prisms, open black circles) and prisms containing O terminated (111) facets (O-Zn-O prisms, open gray circles) are considered individually. The solid black/gray lines correspond to the $1/l_{(111)}$ fit (excluding smaller prisms). The dashed black/gray lines indicate $\Delta\epsilon^{\infty}$ for the Zn-O-Zn and O-Zn-O prisms; the dashed orange line shows their average. The solid orange line finally shows the expected value obtained from the known average surface energies, see Eq. (8).

graphs are shown in Fig. S7 in the Supplemental Material [28]. As to be expected from Eq. (8), the average of $\Delta\epsilon^{\mathrm{exc},\infty}_{\mathrm{Zn\text{-}O\text{-}Zn}}$ and $\Delta\epsilon^{\mathrm{exc},\infty}_{\mathrm{O\text{-}Zn\text{-}O}}$ almost exactly matches $\bar{\sigma}_{(111)} + 1/\sqrt{3}\bar{\sigma}_{(001)}$. The termination dependent variation of the later surface energy is shown in Fig. 5. The surface energy can be generally parameterized as

$$\sigma(\Delta\mu_{\mathrm{O}}) = \sigma_0 + S\Delta\mu_{\mathrm{O}}, \qquad (9)$$

where $\Delta\mu_{\mathrm{O}} = 0$ corresponds to the maximum value allowed for the O chemical potential (see below), σ_0 is the value of σ at $\Delta\mu_{\mathrm{O}} = 0$ and S is the slope. The maximum chemical potential of O is determined via [42]

$$\mu_{\mathrm{O}}^{\mathrm{max}} = \epsilon_{\mathrm{ZnO}} - \epsilon_{\mathrm{Zn}} - h^{\mathrm{f}}_{\mathrm{ZnO}}, \qquad (10)$$

where ϵ_{ZnO} and ϵ_{Zn} are the DFT total energies per f.u. of bulk ZnO and Zn, and $h^{\mathrm{f}}_{\mathrm{ZnO}}$ is the experimental formation energy of ZnO from Zn and O per formula unit ($H^{\mathrm{f}}_{\mathrm{ZnO}} = 350.46 \pm 0.27$ kJ/mol [43]). The minimum value of the O chemical potential is $\mu_{\mathrm{O}}^{\mathrm{max}} = \epsilon_{\mathrm{ZnO}} - \epsilon_{\mathrm{Zn}}$. Table II lists parameters for the two terminations of the zb(001) surface obtained using various functionals.

Figure 6 finally shows the variation of the surface energies of zb(111) and wz(0001) with respect to the O chemical
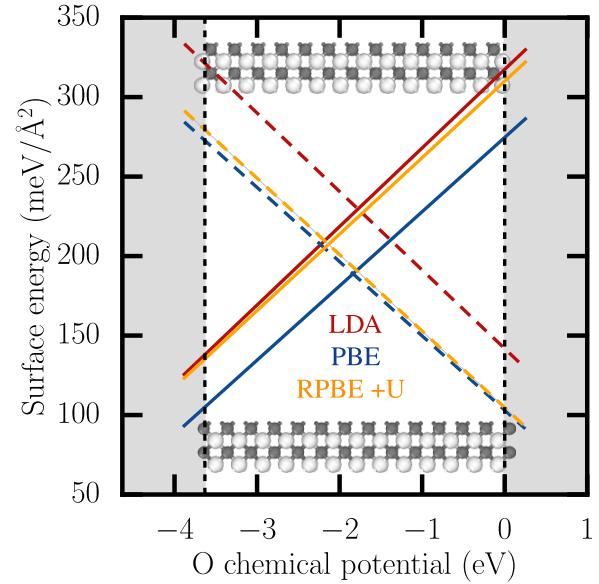

FIG. 5. Surface energy of Zn (solid lines) and O terminated (dashed lines) zb(001) calculated using LDA, PBE, and RPBE+U (from top to bottom). Convergence relative to the slab thickness has been performed. The insets detail two differently terminated slabs.

potential. For wz(0001), the diagram is constructed according to Eq. (4) (evaluated at the equilibrium chemical potential of both surfaces) and by rescaling the slope by the ratio of surface area per atom of zb(111) and wz(0001), $A_{(111)}/A_{(0001)}$. The parameters corresponding to Eq. (9) are again listed in Table II.

TABLE II. Parameterization of surface energies for various XC functionals according to $\sigma(\Delta\mu_{\mathrm{O}}) = \sigma_0 + S\Delta\mu_{\mathrm{O}}$. Here $\Delta\mu_{\mathrm{O}} = 0$ corresponds to the maximum allowed value of the O chemical potential.

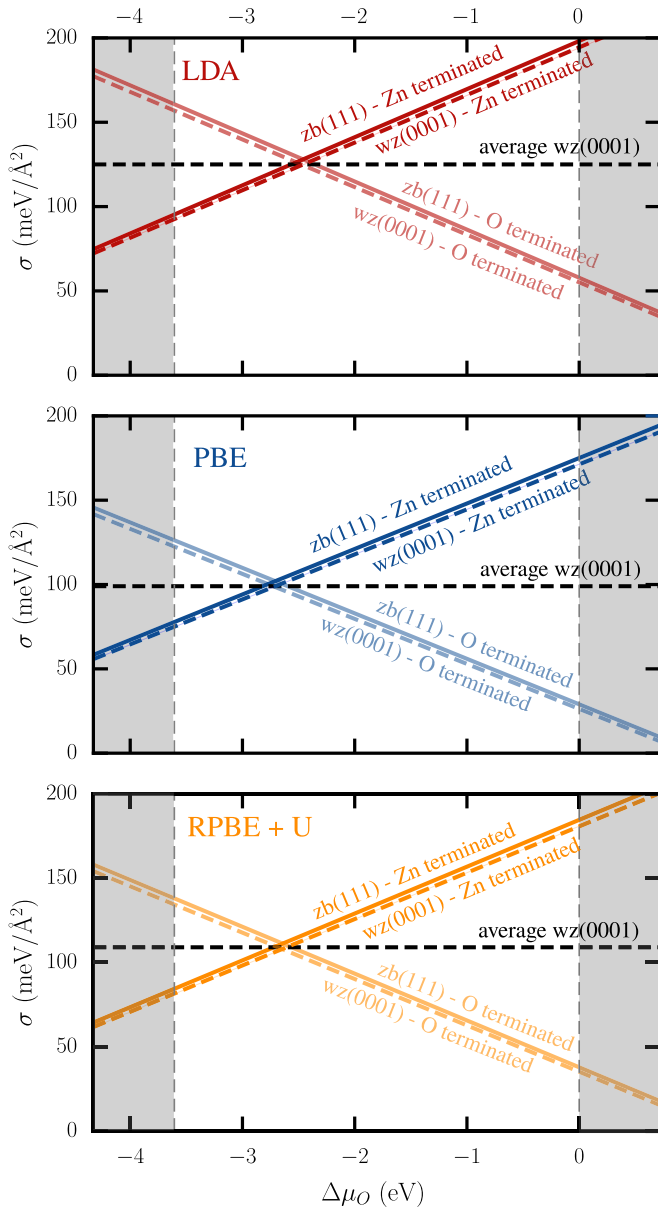| Surface	Termination	σ_0 (meV/Å^2)	S (meV/Å^2/eV)
		LDA	
zb(001)	Zn	318	+49.4
zb(001)	O	142	−49.4
zb(111)	Zn	198	+28.5
zb(111)	O	58	−28.5
wz(0001)	Zn	194	+28.2
wz(0001)	O	55	−28.2
		PBE	
zb(001)	Zn	275	+46.7
zb(001)	O	104	−46.7
zb(111)	Zn	175	+27.0
zb(111)	O	29	−29.0
wz(0001)	Zn	171	+26.7
wz(0001)	O	26	−26.7
		RPBE+U	
zb(001)	Zn	310	+48.1
zb(001)	O	106	−48.1
zb(111)	Zn	184	+27.8
zb(111)	O	38	−27.8
wz(0001)	Zn	181	+27.5
wz(0001)	O	35	−27.5

FIG. 6. Variation of the surface energy of Zn and O terminated zb(111) and wz(0001) ZnO surfaces calculated using LDA, PBE, and RPBE+U (from top to bottom).

We note that in previous studies, Tang *et al.* [40] and Zhang *et al.* [41] also reported excess energies of individually terminated wz{0001} surfaces. At the maximum O chemical potential and using the PBE functional, they found that the excess of the Zn and O terminated surfaces amounts to roughly 150 meV/Å^2 and 60 meV/Å^2, respectively. The large deviation between our values and theirs originates mainly from the fact that the autors used the DFT total energy of a O$_2$ molecule to determine that maximum O chemical potential. When using the experimental formation energy of bulk wz from the elements, see Eq. (10), this O-rich limit is shifted by ≈1 eV to the right. Using our calculated slopes, this increases/reduces their calculated excess of Zn/O terminated at $\Delta\mu_O$ by roughly 30 meV/Å^2, rendering their numbers and ours comparable within 5 meV/Å^2. Despite this discrepancy,

the difference in the excess between wz and zb calculated by Tang *et al.* agrees with our values.

2. Grain boundary excess energies, continued

We are now in the position to compute absolute GB excess energies of our nonperiodic bicrystal models using Eq. (1) and a correction for the pseudo-H saturation, see Sec. III B in the Supplemental Material [28]. Figure 7 shows the variations of GB energies for the two types of GBs (Zn/Zn and O/O) with different interlayer coverages as functions of the O chemical potential. The limits of the O chemical potentials are chosen as in the case of surface energies.

At both GB types, the models with $\theta = 1/2$ are stable over the entire or at least the largest part of the allowed range of the O chemical potential. This result is independent of the choice of XC functional and will not not altered by considering error bars on the order of ± 5 meV/Å^2 for individual GB energies.

However, at high O chemical potential, predictions from various functionals differ slightly. At the Zn/Zn GB, RPBE+U indicates a stability for GBs with O interlayers of coverage $\theta = 4/7$ for -1 eV $\leqslant \Delta\mu_O \leqslant -0.5$ eV and $\theta = 1$ for $\Delta\mu_O \geqslant -0.5$ eV. The LDA and PBE functionals, only suggest the presence of the $\theta = 1$ for roughly $\Delta\mu_O \geqslant -0.5$ eV. At the O/O GB, LDA indicates a stabilization of the $\theta = 1/3$ IDB at $\Delta\mu_O \leqslant -1$ eV, while PBE indicates an instability of the GB at very high O chemical potential ($\Delta\mu_O \leqslant -0.2$ eV) in favor of separation into to O terminated surfaces ($\theta = 0$). RPBE+U indicates the stability of the $\theta = 1/2$ phase over the entire window.

We emphasize that, despite the inversion of polarization at the IDBs studied here, these systems are by no means high-energy GBs. The constant values of 70–95 meV/Å^2 and 45–90 meV/Å^2 for Zn/Zn and O/O GBs with $\theta = 1/2$ (the range given here is due to different XC functionals) are comparable to or even well below excess energies calculated for other, experimentally observed stoichiometric ZnO GBs, such as $(10\bar{1}0)[10\bar{1}0]\Sigma 1$ (10 meV/Å^2), $(12\bar{3}0)[0001]\Sigma 7$ (80 meV/Å^2), $(10\bar{1}0)[10\bar{1}0]\Sigma 13$ (144 meV/Å^2), $(10\bar{1}0)[10\bar{1}0]\Sigma 19$ (125 meV/Å^2) [20].

B. Atomic structure

Figure 8 (top panels) shows the atomic structure at thermodynamically favored IDBs in more detail. At the $\theta = 1/2$ GBs (columns 1 and 4), all atoms are 4-fold coordinated which clarifies their stability and the fact that their excess energy is independent of the O chemical potential. Effectively, there are no excess atoms since all atoms have the coordination of bulk atoms. The stacking across the GB can be described as $\ldots [AaBb]A - h_1a_1 - H[bBhH]\ldots$ (Zn/Zn) and $\ldots [aAbB]a - H_1A_1 - h[BbHh]\ldots$ (O/O). Here, capital letters denote the site occuptaion of Zn and small letters the site occupation of O. The sequence in brackets represents the bulk unit that periodically repeats away from the GB (indicated by $\ldots$). If present, a subscript label finally indicates how many (out of the four) sites are occupied per unit cell. The Zn/Zn GBs and the O/O GBs are isomorphic, that is, they have essentially the same structure, except that Zn and O switch sites. In the Supplemental Material [28], a more detailed description of the internal u-parameter and bond lengths
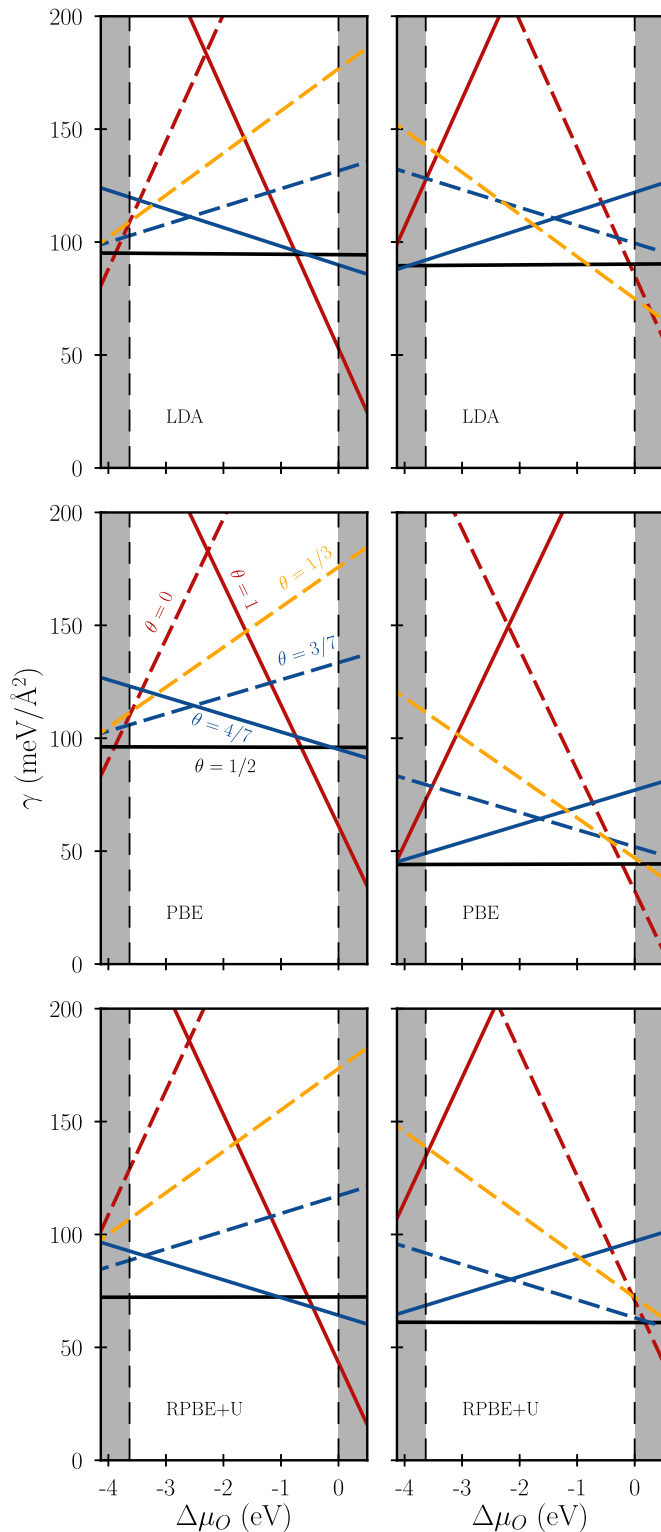
FIG. 7. Grain boundary excess energies for Zn/Zn (left) and O/O (right) IDBs with various coverages of O and Zn interlayers, calculated using LDA, PBE, and RPBE+U (from top to bottom). Independent of the XC functional, the $\theta = 1/2$ IDBs are thermodynamically favored over almost the entire range of the O chemical potential.

and angles is given, see Figs. S8 and S9. Effectively, these GBs correspond to associations of two (2×2) adatom recon-

structed ZnO{0001} surfaces in 1-to-1 correspondence to the (2×2) GaN{0001} reconstruction [44]. This reconstruction cancels the ionic part of the surface (or in this case interface) dipoles generated by cleaving the crystal. Remaining accumulated dipoles from the bulk are canceled via electronic relaxations (polarization charges) and oscillating structural rearrangements directly at the boundary, see Figs. S8 and S9.

Figure 8 also shows the lowest-energy configurations of the Zn/Zn GB with $\theta = 4/7$ and $\theta = 1$ (columns 2 and 3). In both cases, overcoordinated Zn atoms are present, while all O atoms are still 4-fold coordinated. At the $\theta = 1$ GB, the stacking sequence is $\ldots[AaBb]A - a - B[hHbB]\ldots$, so that the interlayer atoms in a are still 4-fold bonded; however, the Zn atoms in the next layer in B sites are 6-fold coordinated. At the $\theta = 4/7$ GB, the stacking sequence cannot be represented in such simple terms. We note that $\theta = 1$ structure coincides with that proposed and investigated by Hoemke *et al.* [27] for the case of Al- and Mn-doped IDBs, both elements preferring 6-fold bonding to O.

C. Electronic structure and response

Figure 8 also shows various electronic aspects of the GB models (exclusively calculated with the RPBE+U functional), such as the layer-averages of the atom-projected density of states (PDOS, with the Fermi level E_F set to the valence-band maximum), Bader excess electrons [45,46] (= # electrons – nominal # electrons in an isolated atom), and effective potentials. The electronic properties were investigated for the fully optimized (stress-free) models as well as for models under compressive and tensile strain. The strained systems were obtained by homogeneously rescaling the atomic positions along the c-axis (fixing the in-plane lattice parameters and thus neglecting lateral contraction), fixing the outermost two atomic layers and letting all other atoms relax. Tensile and compressive strains of 1.3% were applied. These strains correspond to calculated stresses of roughly 2500 MPa (between -2002 MPa and $+2991$ MPa, depending on the IDB and the sign of the applied strain) and are one order of magnitude larger than in experiments.

From the PDOS, we find that apart from the Zn/Zn IDB with O interlayer coverage $\theta = 1$, all IDB models show a semiconducting behavior; the $\theta = 1$, on the other hand possesses a slight metallicity around the 6-fold coordinated Zn layer. The energy gap is hard to resolve in these graphs. A closer inspection, however, shows that this gap does not vary significantly with the individual layer. Moreover, no additional gap states are observed in the vicinity of the GBs. This also applies for energetically less favored systems (not shown in the figure).

Applying a strain has hardly any effect on the electronic structure. In the density of states, only minor changes can be observed. Moreover, these changes appear equally (or even more pronounced) in the bulk regions than close to the GB. Similarly, the calculated Bader charges on individual atoms or the effective potential seen by electrons are hardly affected at by strain. For the $\theta = 1/2$ case, we checked that this holds true also for periodic models (containing two nonequivalent IDBs simultaneously) for strains up to $\pm 2\%$.
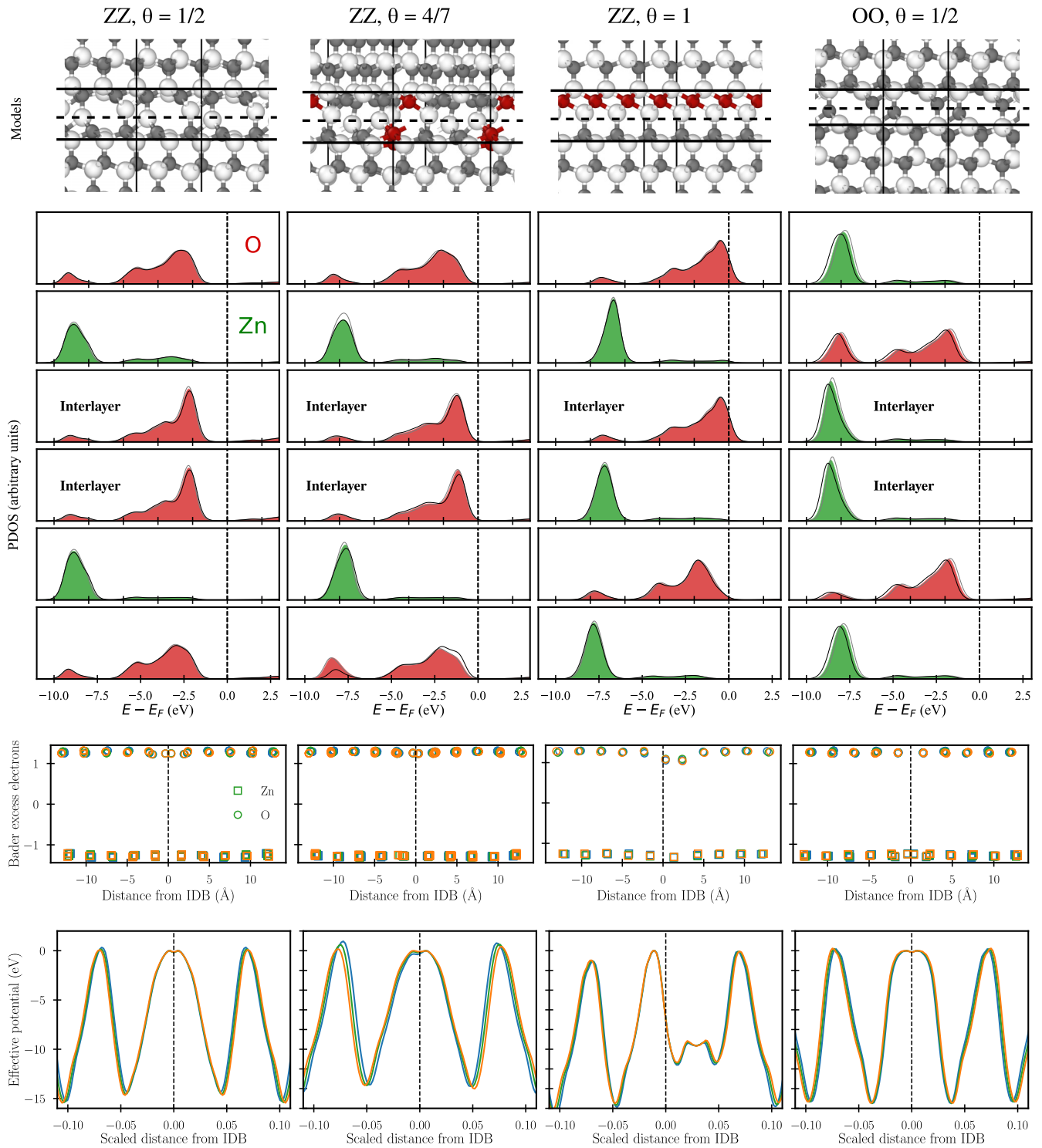
FIG. 8. Atomic and electronic structure of thermodynamically favored Zn/Zn (columns 1–3) and O/O IDBs (column 4). At $\theta = 1/2$ GBs, all atoms are ideally 4-fold coordinated. At Zn/Zn IDBs, systems with overcoordinated Zn ($\theta = 4/7, 1$) may be stabilized at high O chemical potential, compare to Fig. 7. Electronic properties are presented for the stress-free state and at 2500 MPa compressive/tensile stress. In the PDOS, effects of mechanical strain are indicated in black (compressive) and gray (tensile) but are hard to resolve by the eye. In particular, no gap states arise at the IDBs. Similarly, strain has hardly any effect on Bader excess electrons or on effective potentials. Color coding: O and Zn atoms are represented as large light and small dark gray spheres; overcoordinated atoms are colored in red, undercoordinated atoms are not present. Bader charges/effective potential of strain-free (compressively/tensile strained) systems are shown in green (blue/orange).

IV. SUMMARY AND CONCLUSION

In summary, we presented an extensive screening for thermodynamically favorable atomic structures and chemical compositions of wurtzite ZnO {0001} inversion domain boundaries (IDBs) that may appear in piezotronically active ZnO bicrystals [18]. Despite the lack of appropriate symmetries in wurtzite ZnO, GB energies were calculated separately for O/O and Zn/Zn IDBs. This was achieved by using nonperiodic bicrystal setups and approximating the wurtzite {0001} surfaces by corresponding zincblende {111} surfaces; the latter were computed using one-dimensional periodic prism models. We estimate that the error bar introduced by this approximation is within the range of only a few meV/Å^2. Moreover, by comparing LDA, PBE, and RPBE+U, we show that all results are qualitatively largely independent of the particular choice of the exchange-correlation functional.

The favorable models for the Zn/Zn and O/O IDBs are structurally isomorphic over almost the entire range of the O chemical potential μ_O. Their atomic structure is characterized by exclusively 4-fold coordinated atoms with bulk-like bonds even at the GB. Their structure can be represented as a (2×2) IDB with an interlayer of coverage $\theta = 1/2$ and a $\dots [AaBb]A - h_1a_1 - H[bBhH] \dots$ stacking. The corresponding excess energies are comparable to or lower than excess energies of various special GBs discussed in the literature [20].

At higher O chemical potentials and at Zn/Zn GBs, two other GB modifications may appear. At very high O chemical potential, the GB becomes fully decorated with O, leading to 6-fold coordinated Zn in the neighboring layer. For roughly $-1 \leqslant \mu_O \leqslant -0.5$ a more complex structures may arise that may be described as a $\Sigma 7$ twist boundary with an O interlayer of coverage $\theta = 4/7$. However, this prediction is only seen when using the RPBE+U functional; this structure is absent in the LDA or PBE phase diagram. In any case, their electronic properties (density of states, Bader charges, and effective potential) of all these IDB models are similar to those in the bulk. In particular, they do not show a significant repsonse to strain that could rationalize the piezotronic properties of ZnO bicrystals. We thus suggest that the experimentally observed behavior is not an intrinsic property of the pristine IDB, but may only result upon charging the system or upon introducing defects, impurity atoms or dopants.

Nonetheless, the favorable models identified in this work may be useful for comparison with general experimental characterizations of pristine or doped wz ZnO{0001} IDBs [47–50] and for other wz- or zb-type systems, such as, e.g., GaN, AlN, InN, SiC, and so on [51–53], including heterojunctions [54] and ternary systems [55,56] Finally, the models may serve as a starting point for further investigations of strain effects on charged and doped IDBs for improving our understanding of the mechanical tunability of ZnO bicrystals.

ACKNOWLEDGMENT

[1] U. Özgür, Y. I. Alivov, C. Liu, A. Teke, M. A. Reshchikov, S. Doğan, V. Avrutin, S.-J. Cho, and H. Morkoç, A comprehensive review of ZnO materials and devices, J. Appl. Phys. **98**, 041301 (2005).

[2] A. Tsukazaki, A. Ohtomo, T. Onuma, M. Ohtani, T. Makino, M. Sumiya, K. Ohtani, S. F. Chichibu, S. Fuke, Y. Segawa, H. Ohno, H. Koinuma, and M. Kawasaki, Repeated temperature modulation epitaxy for p-type doping and light-emitting diode based on ZnO, Nat. Mater. **4**, 42 (2004).

[3] I.-S. Jeong, J. H. Kim, and S. Im, Ultraviolet-enhanced photodiode employing n-ZnO/p-Si structure, Appl. Phys. Lett. **83**, 2946 (2003).

[4] R. L. Hoffman, B. J. Norris, and J. F. Wager, ZnO-based transparent thin-film transistors, Appl. Phys. Lett. **82**, 733 (2003).

[5] T. K. Gupta, Application of Zinc oxide varistors, J. Am. Ceram. Soc. **73**, 1817 (1990).

[6] X. Wang, J. Zhou, J. Song, J. Liu, N. Xu, and Z. L. Wang, Piezoelectric field effect transistor and nanoforce sensor based on a single ZnO nanowire, Nano Lett. **6**, 2768 (2006).

[7] J. Zhou, Y. Gu, P. Fei, W. Mai, Y. Gao, R. Yang, G. Bao, and Z. L. Wang, Flexible piezotronic strain sensor, Nano Lett. **8**, 3035 (2008).

[8] Y. Gao and Z. L. Wang, Equilibrium potential of free charge carriers in a bent piezoelectric semiconductive nanowire, Nano Lett. **9**, 1103 (2009).

[9] Y. Hu, B. D. B. Klein, Y. Su, S. Niu, Y. Liu, and Z. L. Wang, Temperature dependence of the piezotronic effect in ZnO nanowires, Nano Lett. **13**, 5026 (2013).

[10] Z. Zhang, Q. Liao, X. Zhang, G. Zhang, P. Li, S. Lu, S. Liu, and Y. Zhang, Highly efficient piezotronic strain sensors with symmetrical Schottky contacts on the monopolar surface of ZnO nanobelts, Nanoscale **7**, 1796 (2015).

[11] P. Keil, T. Frömling, A. Klein, J. Rödel, and N. Novak, Piezotronic effect at Schottky barrier of a metal-ZnO single crystal interface, J. Appl. Phys. **121**, 155701 (2017).

[12] P. Keil, R. Baraki, N. Novak, J. Rödel, and T. Frömling, Gauge factors for piezotronic stress sensor in polycrystalline ZnO, J. Phys. D **50**, 175106 (2017).

[13] N. Novak, P. Keil, T. Frömling, F. H. Schader, A. Martin, K. G. Webber, and J. Rödel, Influence of metal/semiconductor interface on attainable piezoelectric and energy harvesting properties of ZnO, Acta Mater. **162**, 277 (2019).

[14] J. Wong and F. P. Bundy, Pressure effects on metal oxide varistors, Appl. Phys. Lett. **29**, 49 (1976).

[15] P. M. Verghese and D. R. Clarke, Piezoelectric contributions to the electrical behavior of ZnO varistors, J. Appl. Phys. **87**, 4430 (2000).

[16] R. Baraki, N. Novak, T. Frömling, T. Granzow, and J. Rödel, Bulk ZnO as piezotronic pressure sensor, Appl. Phys. Lett. **105**, 111604 (2014).

[17] N. Raidl, P. Supancic, R. Danzer, and M. Hofstätter, Piezotronically modified double Schottky barriers in ZnO varistors, Adv. Mater. **27**, 2031 (2015).

[18] P. Keil, M. Trapp, N. Novak, T. Frömling, H.-J. Kleebe, and J. Rödel, Piezotronic tuning of potential barriers in ZnO bicrystals, Adv. Mater. **30**, 1705573 (2018).

[19] G. Blatter and F. Greuter, Carrier transport through grain boundaries in semiconductors, Phys. Rev. B **33**, 3952 (1986).

[20] W. Körner, P. D. Bristowe, and C. Elsässer, Density functional theory study of stoichiometric and nonstoichiometric ZnO grain boundaries, Phys. Rev. B **84**, 045305 (2011).

[21] W. Körner and C. Elsässer, Density functional theory study for polycrystalline ZnO doped with Si or Nb, Phys. Rev. B **83**, 205306 (2011).

[22] J. Wu, X. Tang, F. Long, and B. Tang, Effect of ZnO twin grain boundary on Zn vacancies induced d^0 ferromagnetism: First-principles calculations, Physica Status Solidi (b) **254**, 1600838 (2017).

[23] J. Wu, X. Tang, C. Pu, F. Long, and B. Tang, Twin grain boundary mediated ferromagnetic coupling in co-doped ZnO: First-principles calculations, Solid State Commun. **250**, 41 (2017).

[24] Y. Dai, Z. Zhong, and S. Gong, Effect of ZnO grain boundaries on non-linearity: First-principles calculations, Mater. Res. Express **5**, 065904 (2018).

[25] S. Li, H. Lei, Z. Wang, J. Chen, and P. Ruterana, Energetic and electronic properties of (0001) inversion domain boundaries in ZnO, Physica Status Solidi (b) **255**, 1700429 (2018).

[26] A. B. Yankovich, B. Puchala, F. Wang, J.-H. Seo, D. Morgan, X. Wang, Z. Ma, A. V. Kvit, and P. M. Voyles, Stable p-type conduction from sb-decorated head-to-head basal plane inversion domain boundaries in ZnO nanowires, Nano Lett. **12**, 1311 (2012).

[27] J. Hoemke, E. Tochigi, T. Tohei, H. Yoshida, N. Shibata, Y. Ikuhara, and Y. Sakka, Inversion domain boundaries in mn and al dual-doped ZnO: Atomic structure and electronic properties, J. Am. Ceram. Soc. **100**, 4252 (2017).

[28] See Supplemental Material at http://link.aps.org/supplemental/10.1103/PhysRevMaterials.5.023601 for detailed presentation and analysis of computational paramters, surface saturation, surface energy calculations via prism setups, and structure and energetics of individual grain boundary models.,

[29] G. Kresse and J. Furthmüller, Efficient iterative schemes for *ab initio* total-energy calculations using a plane-wave basis set, Phys. Rev. B **54**, 11169 (1996).

[30] P. E. Blöchl, Projector augmented-wave method, Phys. Rev. B **50**, 17953 (1994).

[31] H. J. Monkhorst and J. D. Pack, Special points for Brillouin-zone integrations, Phys. Rev. B **13**, 5188 (1976).

[32] S. H. Vosko, L. Wilk, and M. Nusair, Accurate spin-dependent electron liquid correlation energies for local spin density calculations: A critical analysis, Can. J. Phys. **58**, 1200 (1980).

[33] J. P. Perdew, K. Burke, and M. Ernzerhof, Generalized Gradient Approximation Made Simple, Phys. Rev. Lett. **77**, 3865 (1996).

[34] Y. Zhang and W. Yang, Comment on Generalized Gradient Approximation Made Simple, Phys. Rev. Lett. **80**, 890 (1998).

[35] B. Hammer, L. B. Hansen, and J. K. Nørskov, Improved adsorption energetics within density-functional theory using revised Perdew-Burke-Ernzerhof functionals, Phys. Rev. B **59**, 7413 (1999).

[36] C. Adamo and V. Barone, Toward reliable density functional methods without adjustable parameters: The PBE0 model, J. Chem. Phys. **110**, 6158 (1999).

[37] P. J. Stephens, F. J. Devlin, C. F. Chabalowski, and M. J. Frisch, *Ab initio* calculation of vibrational absorption and circular dichroism spectra using density functional force fields, J. Phys. Chem. **98**, 11623 (1994).

[38] S. L. Dudarev, G. A. Botton, S. Y. Savrasov, C. J. Humphreys, and A. P. Sutton, Electron-energy-loss spectra and the structural stability of nickel oxide: An LSDA+U study, Phys. Rev. B **57**, 1505 (1998).

[39] M. Christensen, G. Wahnström, C. Allibert, and S. Lay, Quantitative Analysis of WC Grain Shape in Sintered WC-Co Cemented Carbides, Phys. Rev. Lett. **94**, 066105 (2005).

[40] C. Tang, M. J. S. Spencer, and A. S. Barnard, Activity of ZnO polar surfaces: An insight from surface energies, Phys. Chem. Chem. Phys. **16**, 22139 (2014).

[41] J. Zhang, Y. Zhang, K. Tse, B. Deng, H. Xu, and J. Zhu, New approaches for calculating absolute surface energies of Wurtzite (0001)/(000$\bar{1}$): A study of ZnO and gan, J. Appl. Phys. **119**, 205302 (2016).

[42] K. Reuter, C. Stampf, and M. Scheffler, *Ab Initio Atomistic Thermodynamics and Statistical Mechanics of Surface Properties and Functions* (Springer, Dordrecht, The Netherlands, 2005), pp. 149–194.

[43] *NIST Chemistry WebBook, NIST Standard Reference Database Number 69*, edited by P. J. Linstrom and W. G. Mallard (National Institute of Standards and Technology, Gaithersburg, MD, 2005).

[44] Q.-K. Xue, Q. Z. Xue, R. Z. Bakhtizin, Y. Hasegawa, I. S. T. Tsong, T. Sakurai, and T. Ohno, Structures of GaN(0001)-(2×2), −(4×4), and −(5×5) Surface Reconstructions, Phys. Rev. Lett. **82**, 3074 (1999).

[45] R. F. W. Bader, *Atoms in Molecules* (American Cancer Society, Atlanta, 2002).

[46] W. Tang, E. Sanville, and G. Henkelman, A grid-based Bader analysis algorithm without lattice bias, J. Phys.: Condens. Matter **21**, 084204 (2009).

[47] A. Rečnik, N. Daneu, T. Walther, and W. Mader, Structure and chemistry of basal-plane inversion boundaries in antimony oxide-doped Zinc oxide, J. Am. Ceram. Soc. **84**, 2657 (2001).

[48] A. Rečnik, N. Daneu, and S. Bernik, Nucleation and growth of basal-plane inversion boundaries in ZnO, J. Eur. Ceram. Soc. **27**, 1999 (2007).

[49] J. Hoemke, E. Tochigi, T. Tohei, H. Yoshida, N. Shibata, Y. Ikuhara, and Y. Sakka, Inversion domain network stabilization and spinel phase suppression in ZnO, J. Am. Ceram. Soc. **101**, 2616 (2018).

[50] E. Guilmeau, P. Díaz-Chao, O. I. Lebedev, A. Rečnik, M. C. Schäfer, F. Delorme, F. Giovannelli, M. Košir, and S. Bernik, Inversion boundaries and phonon scattering in Ga:ZnO thermoelectric compounds, Inorg. Chem. **56**, 480 (2017).

[51] Y. N. Ahn, S. H. Lee, S. K. Lim, K. J. Woo, and H. Kim, The role of inversion domain boundaries in fabricating crack-free GaN films on sapphire substrates by hydride vapor phase epitaxy, Mater. Sci. Eng.: B **193**, 105 (2015).

[52] S. Li, H. Lei, P.-M. Anglade, J. Chen, and P. Ruterana, Structural stability and electronic properties of the (0001) inversion

domain boundary in III-nitrides, Comput. Mater. Sci. **154**, 152 (2018).

[53] M. Imura, K. Nakajima, M. Liao, Y. Koide, and H. Amano, Microstructure of AlN with two-domain structure on (001) diamond substrate grown by metal-organic vapor phase epitaxy, Diam. Relat. Mater. **19**, 131 (2010).

[54] S. Li, H. Lei, Y. Wang, M. B. Ullah, J. Chen, V. Avrutin, U. Özgür, H. Morkoç, and P. Ruterana, Polarity control within one monolayer at ZnO/GaN heterointerface: (0001) plane inver-sion domain boundary, ACS Appl. Mater. Interfaces **10**, 37651 (2018).

[55] A. P. Goldstein, S. C. Andrews, R. F. Berger, V. R. Radmilovic, J. B. Neaton, and P. Yang, Zigzag inversion domain boundaries in indium Zinc oxide-based nanowires: Structure and formation, ACS Nano **7**, 10747 (2013).

[56] X. Liang and D. R. Clarke, Relation between thermolectric properties and phase equilibria in the ZnO–In$_2$O$_3$ binary sys-tem, Acta Mater. **63**, 191 (2014).